Comparison of Inviscid and Viscous Computations with an Interferometrically Measured Transonic Flow

P.J. Bryanston-Cross* and W.N. Dawes†
Cambridge University, Cambridge, England, U.K.

In order to provide an experimental test case for use with the computer simulation of transonic flowfields, the transonic flow around a wedge profile in a wind tunnel has been measured using holographic interferometry. The quantitative detail provided by the interferogram is compared with the numerical predictions of a two dimensional inviscid time-marching method and a two dimensional Navier-Stokes solver. The a priori Navier-Stokes solution is in agreement with the experimental data. The predictions of the inviscid method can be made to agree with the measurements if the geometrical data used for the computations are modified to represent the presence of the large separated region observed experimentally.

Nomenclature

c_p = specific heat at constant pressure
F,G = ξ- and η-wise flux vectors
H = thin-layer viscous stress term
J^{-1} = area Jacobian, $X_\xi Y_\eta - X_\eta Y_\xi$
L = wedge ramp length
M = Mach number
p = static pressure
P_{0l} = inlet total pressure
Re = Reynolds number
t = time
T_0 = total temperature
U = state vector $(\rho, \rho u, \rho v)^T$
u,v, = X- and Y-wise Cartesian velocity components
$\bar{u}$ = contravariant velocity component, $= \xi_X u + \xi_Y v$
$\bar{v}$ = contravariant velocity component, $= \eta_X u + \eta_Y v$
X,Y = coordinates in the physical plane
ξ,η = coordinates in the computational plane
γ = ratio of specific heats
μ = dimensionless viscosity coefficient
ρ = density
ρ_l = inlet density

Introduction

In recent years there has been rapidly increasing interest in the computer simulation of transonic flowfields. Much progress has been made with calculation methods for both inviscid flows (governed by the Euler equations) and flows in which the effects of viscosity have varying degrees of influence (governed by various versions of the Navier-Stokes equations). Currently, quite complex flowfields can be attempted using the most modern scientific computers.[1-4]

The objectives of this paper are twofold. First, interferometric measurements of a complex transonic flow are presented as a test case to help the development of flow calculation codes. Second, two new codes are applied to this test case and their performances discussed. The transonic test case is the flow around a simple wedge profile in a supersonic wind tunnel. A holographic interferogram of the flow is shown in Fig. 1 and a description of the flow in Fig. 2.

The experimental technique of holographic interferometry provides quantitative detail and gives a precise picture of the positions and strengths of both the shocks and the expansions and visualizes the large embedded separated flow region (with the separation point clearly shown). Measurements were also made using a two-spot laser anemometer to confirm the Mach numbers directly ahead and following the wedge leading-edge shock.

The flowfield contains a number of key features to test computational flow modeling. In particular, there is a range of shock types and a large embedded separation region that significantly modifies the character of the flow. All of these flow features interact and each must be adequately modeled by any computer code in order to give an acceptable overall prediction of the flow.

The flowfield was computed using a two-dimensional inviscid time-marching method and by a two-dimensional Navier-Stokes solver. The Navier-Stokes solution is in fair agreement with the measurements but the inviscid solution can only be made to agree if changes are made to the geometrical data used in the calculation so as to represent the considerable displacement effect of the embedded separation bubble.

Wedge Experiment

The wind tunnel used in this experiment was operated with a stagnation pressure of 200 kPa and a stagnation temperature of 293 K, as shown in Table 1. The air was accelerated through a two-dimensional convergent-divergent passage and exhausted directly into the atmosphere. For this particular experiment the flow was turned through a 90 deg bend during the contraction stage. However, because of the use of flow straighteners in the bend and the following acceleration to supersonic flow the asymmetry present in the divergent part of the flow is small. The width of the tunnel section was only 35.6 mm; although it may be thought that this would lead to a loss of two-dimensionality, within the limits of the experiment the major features of the flow were found to be two-dimensional. This was confirmed by making a series of holograms specifically to visualize three-dimensionality in the flow. In particular, the shock and separated regions were seen to lie in a straight line across the tunnel with only a small amount of curvature (approximately 5% of the span) being produced at the tunnel side walls. The 9 deg wedge angle of the test body was calculated to produce a strong leading edge shock at an inlet Mach number of 1.45.

Holographic Interferometer

The image plane holographic interferometer used in this experiment was a derivative of a previous design described in detail in Ref. 5.

A JK 2000 series ruby pulse laser mounted upon the interferometer framework produced a 1.2 J, 30-ηs-long pulse of

Received March 18, 1983; revision received May 21, 1984.

*Central Electricity Generating Board. Research Fellow, Whittle Laboratory.
†Senior Assistant in Research, Whittle Laboratory.

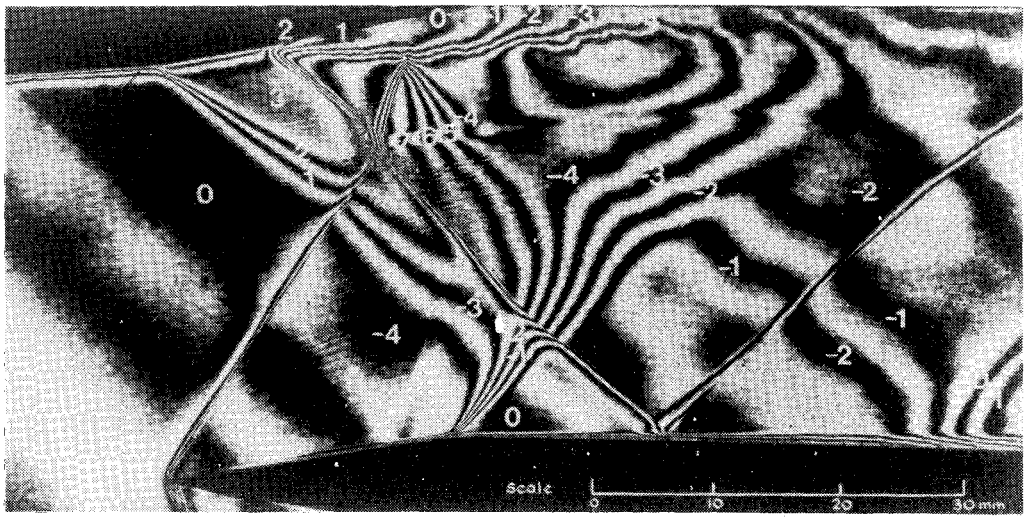

Fig. 1 Image plane hologram of wedge flow.

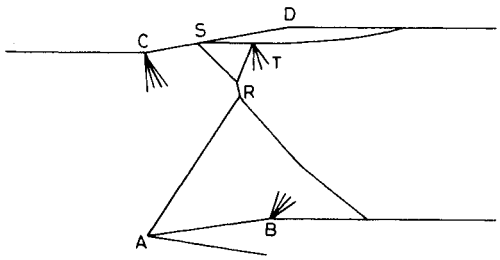

A Leading edge
B Expansion due to change in angle of the wedge profile
C Expansion
D Change in side wall profile angle
R Reflection of leading edge shock
S Point of separation and the foot of a shock
T Expansion following a shock

Fig. 2 Description of flow.

coherent light. The output from the laser was split into two parts, 4% forming the reference beam, the remainder the sample beam. The sample beam was first attenuated by 80% using neutral density filters, expanded through a spatial filter and collimated through a 127-mm-diam, 635-mm focal length planoconvex lens. The collimated beam was then passed through the test section and imaged using a matching lens onto a holographic plate. The image plane of this lens was chosen to minimize the effects of diffraction and refraction. The undiverged reference beam was kept as close as possible to the sample beam, without passing it through the test section. On the far side of the test section it was also expanded through a spatial filter and then combined with the sample beam onto the holographic plate.

The resulting image plane hologram is shown in Fig. 1. A more detailed description of the techniques used in the interpretation of interferometric fringes has been given in Ref. 5. In the wedge flow case laser anemometry was used to measure the flow directly upstream of the shock, and by using the isentropic flow relationships a flow density and Mach number could be associated with the dark fringe labelled 0 in Fig. 1. Although it was not possible to count fringes through the shock, fringes have been counted in the viscous region along the side of the tunnel. These fringes have then been followed back into the mainstream flow downstream of the shock. It was then possible to follow the fringe 0 found at the limit of the profile surface Prandtl-Meyer expansion and count back down to the fringe of order -4.5 ($M=1.10$) directly after the leading-edge profile shock. Shock tables predict a Mach number value of $M=1.09$ for this region. The Mach number distribution calculated from the image plane hologram is shown in Fig. 3.

Table 1 Operating conditions

Continuously running tunnel
Stagnation pressure $P_0=200$ kPa
Stagnation temperature $T_0=293$ K
Re based on wedge ramp length and exit conditions $\cong 2\times 10^5$
Exit condition, to ambient air
Width of tunnel = 35.6 mm
Angle of wedge = 9 deg
½ thickness of wedge = 3.5 mm
Total height of tunnel = 68.5 mm
Length of test section = 81.3 mm

Description of the Flow

A description of the flow is sketched in Fig. 2.

Wedge Surface

The flow approaches the leading edge, A, with a Mach number of 1.45. It then forms a leading-edge shock that reduces its Mach number to 1.09 and turns to run parallel with the profile surface. Upon reaching the top of the profile the flow again changes direction via a Prandtl-Meyer expansion, B. This expansion accelerates the flow almost to its original Mach number. The flow then experiences a weak reflected shock generated at R and continues reaccelerating toward its original Mach number.

Tunnel Wall Surface

The flow along this surface presents a more complicated picture. The flow here first experiences a Prandtl-Meyer expansion around the corner C, increasing its Mach number to about 1.8. Between corners and C and D the tunnel end wall boundary layer separates from the wall and the consequent change of flow direction generates an oblique shock reducing the Mach number to 1.3, on the boundary of the separated region. The continuation of the bow shock then reaches the separated region and, because it is presented with a constant pressure boundary, it is reflected as an expansion wave leaving an almost constant Mach number of 1.3 on the boundary between the separated region and the mainflow.

Computational Results

The complex flow pattern clearly presents a formidable challenge to numerical methods of flow calculation. The significant effect of the separation on the end wall suggests that the flow can only be simulated by a fully viscous flow calculation. Viscous-inviscid interaction types of calculation (e.g., Ref. 6) are thought unlikely to be able to cope with such extensive regions of separated flow.

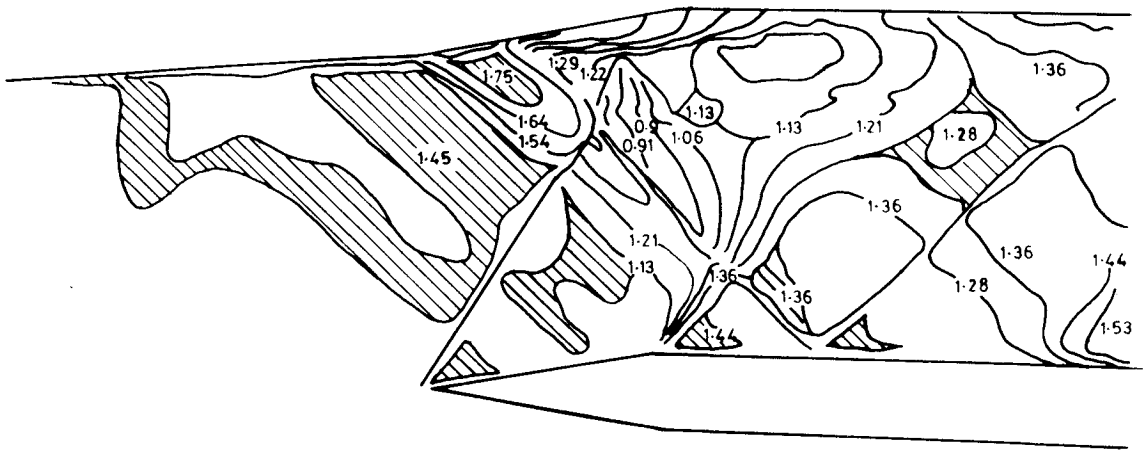

Fig. 3 Mach number distribution calculated from image plane hologram.

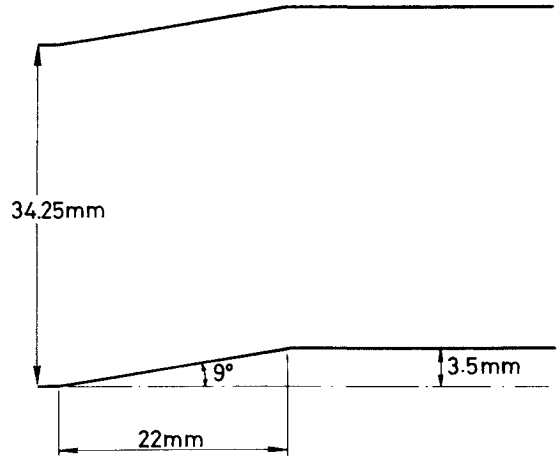

Fig. 4 Basic cascade representing the upper half of the flow channel.

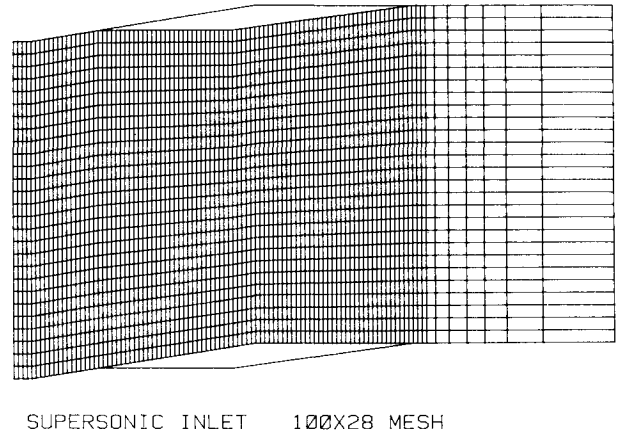

Fig. 5 The grid used for the inviscid calculations.

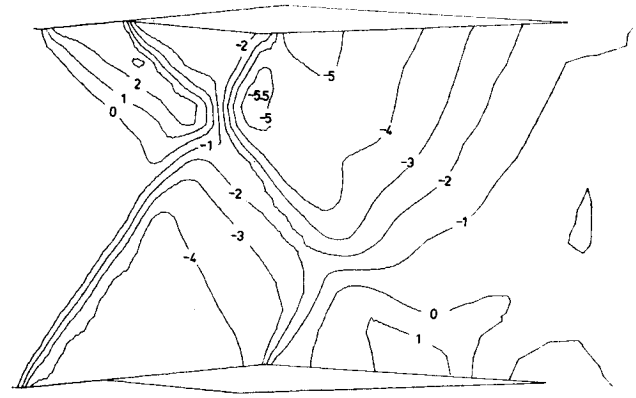

Fig. 6 Density contours calculated using the inviscid method.

At first sight it appears as if an exact prediction of the inviscid flowfield could be obtained easily by the steady supersonic method of characteristics. This would be the case if the bow shock met the walls exactly at the corner (point D in Fig. 2). However, this shock is turned toward the flow direction by the expansion from point C. Simple reflection from the end wall is no longer possible and a Mach reflection, with a normal shock at the wall, results. As the flow near the wall is subsonic after the Mach reflection, a solution by the steady supersonic method of characteristics is no longer possible. As a result, even a prediction of the inviscid flow becomes a difficult task, only possible by numerical means. However, some exact results can still be obtained from the method of characteristics: 1) $M = 1.093$ along AB; 2) $M = 1.441$ immediately downstream of point B, and 3) $M = 1.748$ along DC.

Inviscid Flow Calculation

The method used to predict the inviscid flow was the improved version of Denton's two-dimensional[7] time-marching method for turbomachinery cascades. This method time marches the inviscid Euler equations, expressed in finite volume form, forward from an initial guess to a converged steady solution. This easily can be applied to the geometry concerned where the profile of the tunnel wall surface matches that of the wedge surface. One half of the symmetrical flow channel has then been treated as the flow between an infinite cascade of zero thickness blades. The cascade geometry is shown in Fig. 4.

A comparatively fine 100×28 point grid was used for all solutions, with the points evenly spaced across the pitch and along the blade surfaces but with the spacing increased toward the up- and downstream boundaries. The grid is shown in Fig. 5. With this grid solutions were obtained in about 500 time steps and 3 min CPU time on an IBM 370-165.

The large separated region observed in the experiment can be modeled, to some extent, by modifying the basic cascade geometry by adding thickness to the blades. In order to model the separated region by this new solid boundary it is necessary for the boundary to change direction whenever it meets a wave so that the wave can be reflected with a change of sign and constant pressure on the solid boundary. After several attempts the profile shown in Fig. 6 emerged as that best able to model the measured flow. The thickness distribution starts at the measured point of separation (S) in Fig. 2 and initially the boundary is sloped downward at 2 deg in order to produce the correct shock strength at S. The boundary undergoes an abrupt change of direction at T in order to reflect the incident bow shock as an expansion. The thickness distribution is then gradually closed toward the downstream boundary to represent the reduction in displacement thickness associated with mixing between separated and mainstream fluid.

The flow pattern calculated in this way (Fig. 6) bears a remarkable resemblance to that measured. Although this agreement was only produced by making use of the experimental result to choose the shape of the separated region, it does demonstrate the ability of the inviscid method to predict very complex shock and expansion patterns given the correct geometry. Note that the flow in the region of point R in Fig. 2 is both predicted and measured to be subsonic, so that the complex flow could not have been predicted by the steady supersonic method of characteristics.

Viscous Flow Calculation

Viscous flow calculations were made using a compressible Navier-Stokes solver currently under development by the second author. Full details of the Navier-Stokes solver will be published in a forthcoming paper; only a brief outline of the numerical algorithms will be presented here. The flow equations used are the two-dimensional, isenthalpic, thin-layer Navier-Stokes equations, subjected to general coordinate transformation, but kept in strong conservation form. The flow equations, suitably nondimensionalized, are[8,10]

$$\frac{\partial U}{\partial t}+\frac{\partial F}{\partial \xi}+\frac{\partial G}{\partial \eta}=\frac{1}{Re}\frac{\partial H}{\partial \eta} \tag{1}$$

where: $\xi=\xi(X,Y)$, $\eta=\eta(X,Y,)$

$$U=J^{-1}\begin{bmatrix}\rho\\ \rho u\\ \rho v\end{bmatrix} \quad F=J^{-1}\left[\bar{u}\begin{pmatrix}\rho\\ \rho u\\ \rho v\end{pmatrix}+p\begin{pmatrix}0\\ \xi_x\\ \xi_y\end{pmatrix}\right]$$

$$G=J^{-1}\left[\bar{v}\begin{pmatrix}\rho\\ \rho u\\ \rho v\end{pmatrix}+p\begin{pmatrix}0\\ \eta_x\\ \eta_y\end{pmatrix}\right]$$

$$H=J^{-1}\begin{bmatrix}0\\ \mu(\frac{4}{3}\eta_X^2+\eta_y^2)\partial_\eta u+\mu(\eta_x\eta_y/3)\partial_\eta v\\ \mu(\eta_x\eta_y/3)\partial_\eta u+\mu(\eta_x^2+\frac{4}{3}\eta_y^2)\partial_\eta v\end{bmatrix}$$

In the above, ρ is the density, and p the pressure, given in isenthalpic flow by

$$p=\frac{\gamma-1}{2}\rho\left(c_pT_0-\frac{1}{2}(u^2+v^2)\right) \tag{2}$$

T_0 is the constant total temperature, u and v the Cartesian velocity components, μ the nondimensionalized coefficient of viscosity, and Re the Reynolds number (based on appropriate reference quantities). The contravariant velocities are defined by

$$\bar{u}=\xi_x u+\xi_y v, \qquad \bar{v}=\eta_x u+\eta_y v \tag{3}$$

and the metrics and area Jacobian associated with the coordinate transformation are

$$J^{-1}=X_\xi Y_\eta-X_\eta Y_\xi=1/(\xi_x\eta_y-\xi_y\eta_x)$$

$$\xi_x=JY_\eta \qquad \eta_x=-JY_\xi$$

$$\xi_y=-JX_\eta \qquad \eta_y=JX_\xi \tag{4}$$

A general coordinate transformation is employed so that a body-fitted mesh system in the physical XY plane may be mapped (usually numerically) to a convenient rectangular computation ξ-η plane. The use of a body-fitted mesh allows accurate resolution of solid boundaries, like blade surfaces, with their associated steep velocity gradients. This transformed coordinate approach is directly analogous to the use of a finite volume discretisation in the physical plane.

Since computational power is rarely available to resolve the viscous stress terms in more than one coordinate direction, it is assumed that solid boundaries are coincident with one or more $\eta=$const lines and that only the viscous gradients in the η direction will be resolved. This means that a fine grid need only be used in the η direction near solid boundaries, saving much computer storage and computational time. All viscous terms containing ξ derivatives are neglected as the grid spacing used in directions parallel to solid boundaries is too coarse to resolve them. The retained viscous terms are shown as the right-hand side of Eq. (1). This "thin-layer" approximation[10] is not a necessary assumption, but is made purely in the interests of economy. It should be noted that full elliptic influence of the pressure field is retained in the flux vectors F and G on the left-hand side of Eq. (1).

The dimensionless viscosity coefficient μ is expressed as the sum of laminar and turbulent coefficients. The turbulent coefficient is taken from a simple algebraic eddy viscosity model[11] based on Prandtl's mixing-length theory as modified by van Driest.

A coupled fully implicit numerical algorithm is used to time march the flow equations. The algorithm is an extension of that presented by Dawes.[12] The flow equations are replaced by a set of finite difference equations (with full conservation form retained). The spatial flux derivatives are represented at the implicit time level by appropriate first-order accurate one-sided difference operators. These one-sided operators are formulated in accordance with the concepts of flux-vector splitting[13] to retain the proper numerical domain of dependence within the algorithm. Correction terms are added to the algorithm at the explicit time level so that a converged steady solution is effectively discretized using second-order accurate centered difference operators.

The relationship between the spatial operators and the correction terms may be illustrated considering the simple one-dimensional flow equation,

$$\frac{\partial U}{\partial t}+\frac{\partial F}{\partial X}=0 \tag{5}$$

The present algorithm time marches this as,

$$\frac{\partial U}{\partial t}+\delta_x^u F^{n+1}=\{\delta_x^u F-\delta_x^c F\}^n \tag{6}$$

where δ_x^u represents an appropriate one-sided operator, as discussed above, δ_x^c represents the usual centered difference operator (second-order accurate) and $\{\ldots\}$ represents the correction term. In a converged steady state, $\partial U/\partial t\to 0$, $F^{n+1}\to F^n$ so that $\delta_x^c F\to 0$, the desired result.

The idea of correcting a stable but low accuracy time evolution to attain an accurate converged solution has been used in the past in the context of an explicit Euler equation solver[14] and as a technique in the solution of banded sets of difference equations.[15] However, to the present authors' knowledge, this is the first time such a technique has been used as the basis for an implicit algorithm solving the compressible Navier-Stokes equations.

Terms involving nonlinearities at the implicit time level are linearized by Taylor expansion in time from the known time level and the algorithm recast, for convenience, in delta form. This results in a coupled set of linear matrix-vector equations which are solved at each time step for the flow variables at the new time level. Since the difference operators at the implicit time-level are all one-sided, the implicit coefficient matrix can be factored into lower and upper block triangular matrices[16] which are trivially and noniteratively solved by 2 two-

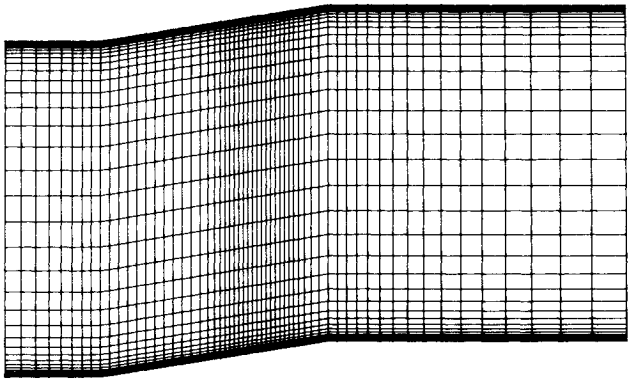

Fig. 7 The grid used for the viscous calculations.

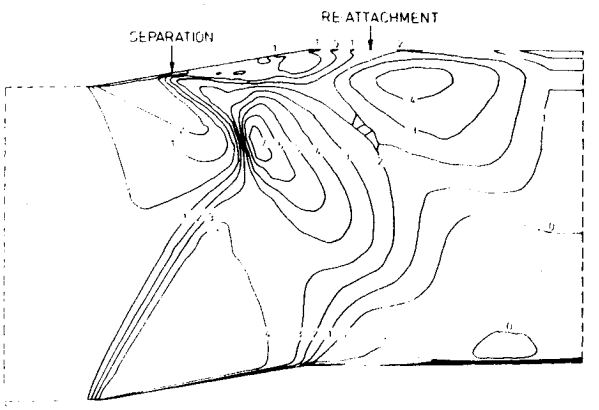

Fig. 8 Density contours calculated using the viscous method.

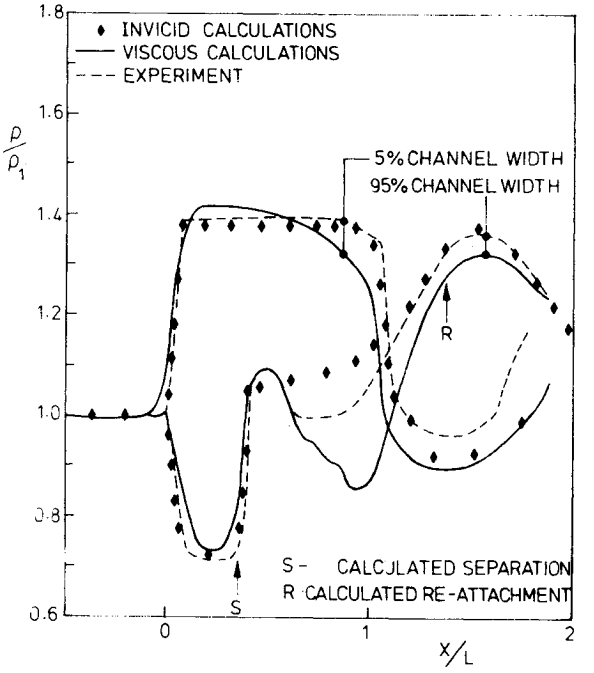

Fig. 9 Plot of measured and calculated density distribution around the channel profile.

dimensional sweeps. The algorithm is applied with spatially varying time steps as a simple way of conditioning the implicit coefficient matrix, reducing its stiffness and speeding convergence.[17] The use of "delta" form removes any dependence of the converged steady state on the size of time step used to reach it.[13]

For reliable practical computations it is desirable to introduce smoothing operators at both implicit and explicit time levels. One-sided Saul'ev-type smoothing operators[18] are introduced conveniently into the factored matrix structure of the implicit time-level of the algorithm. Smoothing operators of the form recommended by Shamroth et al. are added to the explicit time level of the algorithm. These smoothing operators are set to zero locally if the local cell Reynolds number is less than a specified value (typically 10-50); otherwise the smoothing operators introduce just sufficient numerical smoothing to reduce the cell Reynolds number to the specified value. The use of this type of smoothing operator is simply a recognition of the fact that a finite difference mesh can satisfactorily resolve the gradients in a flowfield only if the cell Reynolds number is relatively low.[19] If the cell Reynolds number is too high then short wavelength "wiggles" appear in the solution, indicating the presence of gradients too steep to resolve. In practice, of course, as fine a mesh as can be afforded is used so that regions dominated by physical viscous effects are adequately resolved (and the explicit smoothing operators thus set to zero).

At the moment the program is coded for application to two-dimensional turbomachinery cascades and so it was applied to the present wedge geometry in the same way as the inviscid flow calculation method. However, for these calculations the basic cascade geometry, Fig. 4, was *not* altered by the addition of any thickness. Conventional boundary conditions were used. The blade surfaces are modeled with zero tangential and transverse velocities and zero transverse pressure gradient. Inflow and outflow boundaries were modeled by fixing as many flow variables as there were characteristics pointing into the computational domain and extrapolating the remainder.[20] In addition it is appropriate in this case to fix the backpressure downstream of the cascade; the same value as used for the inviscid calculations was taken. The grid used was 60×50 points with the grid spacing exponentially stretched away from the blade surfaces. The transverse grid spacing at the blade surface is chosen to match the Reynolds number[21] and, in this case, was about 2×10^{-4} of the wedge ramp length. The grid was constructed to have a similar cell size over the main body of the flowfield as that used with the inviscid computations with similar streamwise grid spacing. However, many more grid lines were used near the two solid boundaries to resolve the boundary-layer structures. The grid is shown in Fig. 7. On this grid a solution was obtained in about 900 time steps, using about 22 min of IBM 3081 time. The computed flowfield is presented in Fig. 8 in the form of density contours; the contours have been chosen with values corresponding to the density fringes in the interferogram.

It should be pointed out that since the blade leading edge was taken as shown in Fig. 4, i.e., at the furthest upstream point of the wedge profile, the boundary layer on the wind tunnel wall surface (see Fig. 1) is not modeled correctly. Nevertheless, as can be seen from Fig. 8, the computed flow has a striking resemblance to that measured. Separation of the channel wall boundary layer at the upstream foot of the λ-shock is clearly visible. Reattachment occurs at some location downstream of the corner. The region of subsonic flow downstream of the near normal shock associated with the Mach reflection is well represented.

The densities calculated along 5 and 95% of the channel width are shown in Fig. 9 and are compared with the measured values. Values along the channel walls themselves are not used, since it is very difficult to count the fringes through the boundary layers. The calculated separation and reattachment are shown; precise measured values cannot be found from the interferogram. Agreement between calculated and measured densities along the 95% channel width line are good except in the region of the λ-shock/boundary-layer interaction. The discrepancy here is almost certainly due to the simple equilibrium turbulence model used in the calculations failing to represent the strong nonequilibrium nature of the interac-

tion and the downstream relaxation of turbulence properties. Currently, effort is being devoted to see if the turbulence modeling can be improved, perhaps by the inclusion of a transport model for the turbulence properties.

Conclusions

The transonic flow around a wedge profile in a wind tunnel has been measured using holographic interferometry. The high quality of the interferogram allowed quantitative measurements of the Mach number distribution in a complex two-dimensional transonic flow.

The experimental data have been compared with the flowfields computed by a two-dimensional inviscid time-marching method and by a two-dimensional Navier-Stokes solver. It is shown that if simple changes are made to the geometric data used by the inviscid calculation method (to represent the presence of a large separated region observed experimentally) then good agreement can be obtained with the measurements. The a priori Navier-Stokes solution (using, of course, the actual geometrical data) is in good agreement with the experimental data.

Appendix

Table A1 shows how the holographic fringes can be interpreted to give values of absolute density. If the flow is assumed to be isentropic they can also be used to calculate Mach number.

Table A1

Fringe order number	Absolute density, kg/m^3	Mach number based on ρ_{01}
−8	1.67	0.86
−7	1.58	0.93
−6	1.50	1.00
−5	1.41	1.07
−4	1.32	1.14
−3	1.23	1.22
−2	1.15	1.29
−1	1.06	1.37
0	0.98	1.45
1	0.89	1.54
2	0.80	1.64
3	0.71	1.75

[a] ρ_{01} = preshock stagnation density = 2.37 kg/m^3.

Acknowledgments

The authors would like to thank Dr. J.D. Denton for making his new two dimensional time-marching method available for this work and also the Central Electricity Generating Board for their permission to publish the Navier-Stokes calculations which were made at Marchwood Engineering Laboratories by Dr. Dawes. Dr. Dawes is now a Senior Assistant in Research at the Whittle Laboratory, Cambridge. The experimental part of the paper was supported by the Ministry of Defence, Procurement Executive, and carried out by Dr. Bryanston-Cross at Rolls-Royce, Derby. Dr. Bryanston-Cross is now the Central Electricity Generating Board Fellow, Churchill College, Cambridge.

References

[1] Bowditch, D.N., McNally, W.D., Anderson, B.M., Adamczyk, J.J., and Sockol, P.M., "Computational Fluid Mechanics of Internal Flow," NASA CP 2092, 1979.

[2] Peyret, R. and Viviand, H., "Computation of Viscous Compressible Flows based on the Navier-Stokes Equations," AGARD-AG-212, 1975.

[3] Hankey, W.L., Graham, J.E., and Shang, T.S., "Navier-Stokes Solution of a Slender Body of Revolution at Incidence," *AIAA Journal*, Vol. 20, 1982, pp. 776-781.

[4] Hansen, G.A., "Navier-Stokes Solutions for an Axisymmetric Nozzle," *AIAA Journal*, Vol. 20, 1982, pp. 1219-1227.

[5] Bryanston-Cross, P.J., Lang, T., Oldfield, M., and Norton, R., "Interferometric Measurements in a Turbine Cascade using Image-Plane Holography," *Journal of Engineering for Power*, Jan. 1981, pp. 124-131.

[6] Singh, U.K., "Computation of Transonic Flow in Cascades with Shock and Boundary Layer Interaction," *Proceedings, 1st International Conference on Numerical Methods in Laminar and Turbulent Flow*, Swansea, Wales, July 1978.

[7] Denton, J.D., "An Improved Time Marching Method for Turbomachinery Flow Calculation," ASME Paper 82-GT-239, April 1982.

[8] Shamroth, S.J., McDonald, H., and Briley, W.R., "Application of a Navier-Stokes Analysis to Transonic Cascade Flowfields," ASME Paper 82-GT-235, 1982.

[9] Steger, J.L., "Implicit Finite Difference Simulation of the Flow about Arbitrary Geometries with Applications to Airfoils," AIAA Paper 77-669, 1977.

[10] Kutler, P., "Supersonic Flow over Ablated Nose Tips Using an Unsteady Numerical Procedure," AIAA Paper 78-213, 1978.

[11] Waterman, W.F. and Tall, W.A., "Measurement and Prediction of 3D Viscous Flows in Low Aspect Ratio Turbine Nozzles," ASME Paper 76-GT-73, 1976.

[12] Dawes, W.N., "An Efficient Implicit Algorithm for the Equations of 2D Viscous Compressible Flow: Application to Shock-Boundary Layer Interaction," *International Journal of Heat and Fluid Flow*, Vol. 4, March 1983, pp. 17-26.

[13] Beam, R.M., and Warming, R.F., "On the Construction and Application of Implicit Factored Schemes for Conservation Laws," *SIAM-AMS Proceedings*, Vol. 11, 1978, pp. 85-129.

[14] Denton, J.D., "Transonic Flows in Axial Turbomachinery: Extension of the Finite Area Time-Marching Method to 3D," VKI Lecture Series—84, 1975.

[15] Jacobs, D.A.H., "Iterative Replacement Schemes for Complicated Banded Difference Equations," Central Electricity Generating Board, Cambridge, Rept. RD/L/N 1969/75, 1975.

[16] Jameson, A., and Turkel, E., "Implicit Schemes and LU Decompositions," *Mathematics of Computation*, Vol. 37, No. 156, 1981.

[17] McDonald, H., and Briley, W.R., "Computational Fluid Dynamic Aspects of Internal Flows," AIAA Paper 1445, 1975.

[18] MacCormack, R.W., "A Numerical Method for Solving the Equations of Compressible Viscous Flow," AIAA Paper 81-0110, 1981.

[19] Roache, P.J., "Computational Fluid Dynamics," Hermosa Publishing Albuquerque, N. Mex., 1972.

[20] Rudy, D.M., and Strikwerda, J.C., "Boundary Conditions for Subsonic Compressible Navier-Stokes Calculations," *Computers and Fluids*, Vol. 9, 1981, pp. 327-338.

[21] Deiwert, G.S., "High Reynolds' Number Transonic Flow Simulation," *Lecture Notes in Physics, Proceedings of Fourth International Conference on Numerical Methods in Fluid Dynamics*, Springer-Verlag, 1975, pp. 132-137.